ADVANCED HEALTHCARE MATERIALS
www.advhealthmat.de

Modulation of the Tumor Immune Microenvironment by Bi_2Te_3-Au/Pd-Based Theranostic Nanocatalysts Enables Efficient Cancer Therapy

Fengxia Wu, Haoran Chen, Ruiqi Liu, Yongkuan Suo, Qiqing Li, Youlin Zhang, Hongguang Liu, Zhen Cheng, and Yulei Chang**

Nanozymes with multienzyme-mimicking activities have shown great potential in cancer therapy due to their ability to modulate the complex tumor microenvironment (TME). Herein, a second near-infrared (NIR-II) photothermal-nanocatalyst by decorating Bi_2Te_3 nanosheets with ultrasmall Au/Pd bimetallic nanoparticles (Bi_2Te_3-Au/Pd) to reverse the immunosuppressive TME is developed. The peroxidase (POD)-like and catalase (CAT)-like activities, and glutathione (GSH) consumption capacity of Au/Pd modulates the TME by disrupting the intracellular redox homeostasis and relieving hypoxia in the TME. Notably, the amplified oxidative stress induces the accumulation of lipid hydroperoxides (LPO) for enhanced ferroptosis. Moreover, upon NIR-II photoirradiation at 1064 nm, the localized heat generated by Bi_2Te_3 not only directly ablates the cancer cells but also enhances the Au/Pd-mediated catalysis-mediated cancer therapy. Furthermore, both in vitro and in vivo studies confirm that the Bi_2Te_3-Au/Pd nanocatalysts (BAP NCs) can effectively suppress tumor growth by inducing immunogenic cell death (ICD), and suppressing metastasis and recurrence by the synergistic treatment. Overall, this study provides a promising theranostic strategy for effective tumor inhibition.

1. Introduction

The tumor microenvironment (TME), featured by immunosuppression, oxidative stress, hypoxia, acidic pH, overexpression of glutathione (GSH), etc., is a critical factor that promotes therapeutic resistance, tumor recurrence and metastasis, due to the highly heterogeneous nature of the tumor tissues.[1] In order to overcome these challenges, nanozymes with the ability to modulate the TME have been extensively investigated to enable efficient tumor eradication owing to their intrinsic enzyme-like characteristics.[2] Among them, the noble metal-based nanozymes are the most widely studied due to their remarkable optical and electronic properties, as well as excellent biocompatibility.[3] Furthermore, bimetallic nanozymes with core/shell or alloy structure have been demonstrated to show enhanced catalytic performance (synergistic effect) than the corresponding mono-metallic nanoparticles, since their interaction is known to affect the distribution of the d-band electrons.[4] Moreover, they often express multiple enzyme-like activities, such as peroxidase (POD)-, catalase (CAT)- and oxidase-like activities, enabling their significant potential for different biological application.[5] However, in order to enhance the efficacy of nanoenzyme-based tumor catalytic therapy, it is urgent to develop a TME-responsive therapeutic strategy.

Currently, redox nanozymes with POD-like activity and GSH consumption capacity have been employed for efficient cancer treatment by disrupting the intracellular redox homeostasis.[6] Interestingly, GSH depletion inactivates glutathione peroxidase 4 (GPX4), an enzyme that reduces toxic lipid hydroperoxides (LPO) to non-toxic hydroxyl compounds (LOH), and induces ferroptosis in the cells.[7] Ferroptosis is a type of non-apoptotic cell death pathway caused by reactive oxygen species (ROS)-induced lipid peroxidation which usually arises due to the failure of glutathione dependent antioxidant defenses.[8] Notably, the immunosuppressive state can be alleviated through a ferroptosis pathway.[9]

In addition to developing the above-mentioned nanozymes with multi-enzyme activities, it is also necessary to improve their catalytic activity at the target tumor site by introducing other modifications that could enhance their in vivo efficacy, which may

F. Wu, R. Liu, Y. Suo, H. Liu
Institute of Molecular Medicine
College of Life and Health Sciences
Northeastern University
Shenyang, Liaoning 110000, P. R. China
F. Wu, H. Chen, Q. Li, Y. Zhang, Y. Chang
State Key Laboratory of Luminescence and Applications
Changchun Institute of Optics
Fine Mechanics and Physics
Chinese Academy of Sciences
Changchun, Jilin 130033, P. R. China
E-mail: yuleichang@ciomp.ac.cn
Z. Cheng
State Key Laboratory of Drug Research,Molecular Imaging Center
Shanghai Institute of Materia Medica
Chinese Academy of Sciences
Shanghai 201203, P. R. China
E-mail: zcheng@simm.ac.cn

The ORCID identification number(s) for the author(s) of this article can be found under https://doi.org/10.1002/adhm.202200809

DOI: 10.1002/adhm.202200809

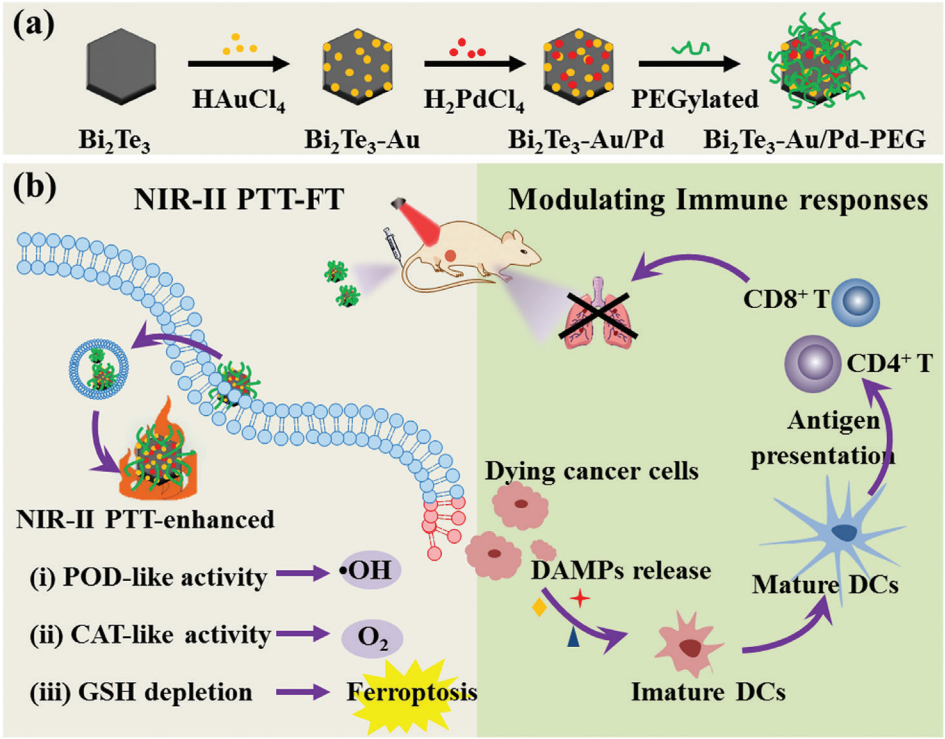

Scheme 1. a) Preparation of the Bi_2Te_3-Au/Pd nanocatalysts (BAP NCs). b) Schematic illustration of the BAP NCs for efficient cancer therapy.

not only enhance the antitumor outcomes but also improve the specificity and biosafety of the therapeutic strategy. Fortunately, temperature is a major factor that regulates the enzyme activity in organisms.[10] Inspired by the photothermal therapy (PTT) principles, a promising near-infrared (NIR) light-triggered tumor therapeutic approach utilizes photothermal agents to convert the harvested photons to generate appropriate local heat to ablate the tumors and simultaneously modulate the catalytic activity thermally.[11] Noticeably, PTT also alleviates the immunosuppressive state and induces immunogenic cell death (ICD) for effective synergistic anticancer therapy.[12]

Here, we developed theranostic nanocatalysts for NIR-II PTT/FT (photothermal therapy/ferroptosis therapy) synergistic therapy (**Scheme 1**). Specifically, gold-palladium bimetallic nanozyme (Au/Pd) with POD- and CAT-like activities were grown in situ on the Bi_2Te_3 nanosheets (named BAP NCs). The Bi_2Te_3 nanosheets provided enough space for the deposition of Au/Pd to avoid aggregation. Additionally, the high loading ability and ultrasmall size of Au/Pd was able to achieve superior antitumor effects due to its larger specific surface area and more exposed active sites.[2a,13] Taking advantage of NIR-II triggered PTT mediated by the strong optical absorption of the Bi_2Te_3 nanosheets, photothermal-augmented ROS generation, and GSH depletion were realized to obtain enhanced therapeutic efficacy. Meanwhile, Au/Pd also exhibited CAT-like activity, which catalyzed the decomposition of H_2O_2 into O_2 to suppress hypoxia in the TME. More importantly, after the NIR-II PTT/FT synergistic treatment, the dying cells elicited ICD by secreting damage-associated molecular patterns (DAMPs) to induce the maturation of dendritic cells (DCs), promote cytokine secretion, and the activation of T cells for reprogramming the immunosuppressive TME.[14]

2. Results and Discussion

2.1. Preparation and Characterization of the BAP NCs

The synthesis of BAP NCs is depicted in Scheme 1a. First, the Bi_2Te_3 nanosheets were synthesized by the solvothermal method according to the previously published reports.[15] The transmission electron microscope (TEM) images (**Figure 1**a) showed that the Bi_2Te_3 nanosheets were monodispersed with the lateral dimension of ≈200 nm, and the high-resolution TEM (HRTEM) image showed the lattice fringes with a d-spacing of 0.219 nm, which matched well with the (110) crystal plane of Bi_2Te_3 (Figure 1a, inset). The powder X-ray diffraction (XRD) pattern showed that the diffraction peaks were consistent with the JCPDS Card (15-0863) (Figure 1e).[16] As shown in the TEM image of Bi_2Te_3-Au, the Au NPs were uniformly distributed on the Bi_2Te_3 nanosheets (Figure S1, Supporting Information). Afterward, the Pd NPs were deposited on the Bi_2Te_3-Au NCs to form BAP NCs, which was confirmed by the TEM image (Figure 1b), showing that the Au/Pd NPs were homogeneously distributed on the Bi_2Te_3 nanosheets.[17] A co-existing polycrystalline phase could be observed in the HRTEM image of the BAP NCs (Figure 1c), with two different fringe distances of 0.238 and 0.224 nm, corresponding to the (111) planes of Au and Pd, respectively.[18] The high-angle annular dark fields scanning TEM (HAADF-STEM) image and energy dispersive X-ray (EDS) spectroscopy mapping images and the energy dispersive spectra (EDX) confirmed the co-existence of Bi, Te, Au, and Pd elements (Figure 1d; Figure S2, Supporting Information). Notably, there were no Pd diffraction peaks in the XRD pattern of the BAP NCs, which could be due to the low content (2.68%) or ultrasmall diameter of the

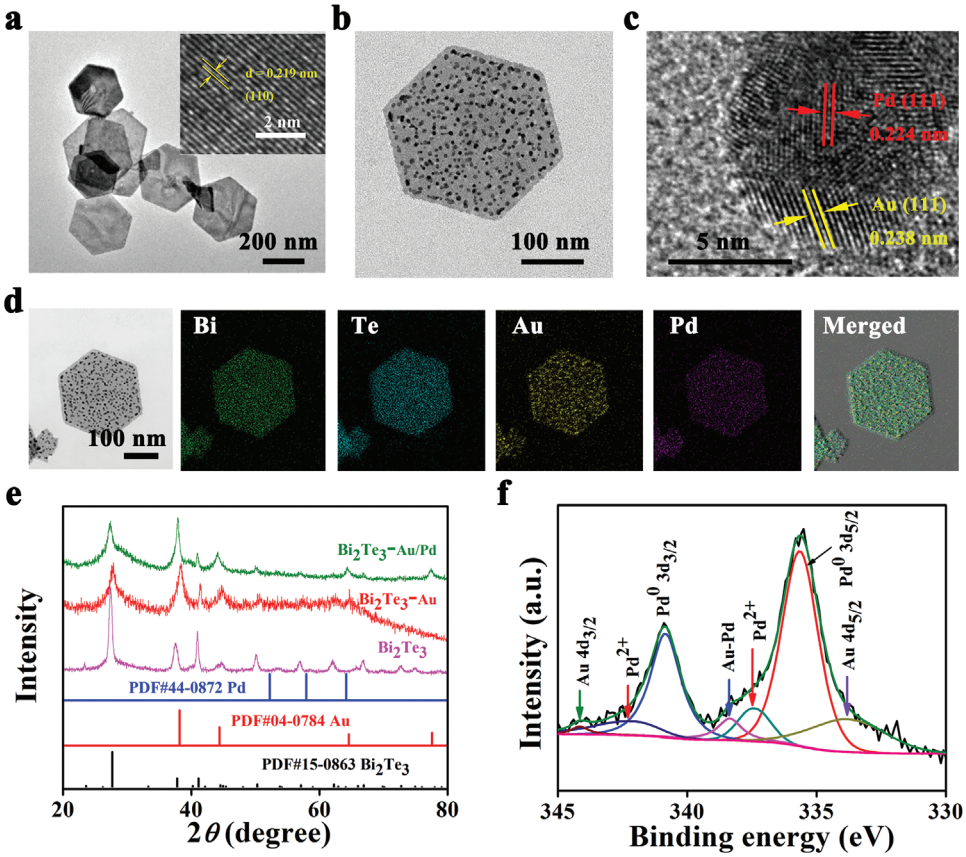

Figure 1. Characterization of the BAP NCs. a) TEM and HRTEM image (inset) of the Bi_2Te_3 nanosheets. b) TEM image of the BAP NCs. c) HRTEM image of the BAP NCs. d) EDS element mapping images of the BAP NCs. e) XRD patterns of Bi_2Te_3 (pink line), Bi_2Te_3-Au (red line), and the BAP NCs (green line). f) High-resolution XPS spectra of Pd 3d for the BAP NCs.

Pd NPs (Figure 1e; Table S1, Supporting Information). Moreover, the X-ray photoelectron spectrum (XPS) survey of the BAP NCs also confirmed the existence of Bi, Te, Au, and Pd elements (Figure S3-iii, Supporting Information). Additional Au peaks (Au 4d and Au 4f) and Pd peaks (Pd 3d) were observed, as shown in Figure S3-ii,iii, Supporting Information, confirming the successful deposition of Au/Pd on the Bi_2Te_3 nanosheets. From the high-resolution XPS spectra shown in Figure S4, Supporting Information, a slight deviation could be observed in the Bi 4f and Te 3d peaks among Bi_2Te_3, Bi_2Te_3-Au and BAP NCs, which could be attributed to the electronic interaction caused by Au/Pd deposition. Impressively, there was a positive shift of the Au 4f peaks by 0.20 eV in the XPS spectrum of the BAP NCs compared to that of the Bi_2Te_3-Au (Figure S5, Supporting Information) spectrum. As shown in Figure 1f, the binding energy values of Pd 3d overlapped with that of Au 4d in the BAP NCs, and the peaks of the binding energies at 335.6 and 340.9 eV could be attributed to Pd^0, an obvious deviation (0.3 eV) was observed from the standard values for Pd (335.3 and 340.6 eV). Such a positive shift of Pd 3d peaks could be attributed to the electronic interaction between Pd and Au.[19] Additionally, the peaks at 337.4 and 342.8 eV were assigned to Pd^{2+}, which could be ascribed to the easily oxidizable nature of Pd atoms in the air.[19b] The above results indicated the successful synthesis of the BAP NCs.

2.2. Photothermal Characteristics of the BAP NCs

As shown in **Figure 2**a, the UV–vis–NIR spectra of BAP NCs exhibited broad absorption in the NIR-II region, and the absorption intensity increased linearly with the increase in the concentration of the BAP NCs, demonstrating their excellent dispersibility. The extinction coefficient (ϵ) was calculated as 8.26 L g^{-1} cm^{-1} at 1064 nm by the Lambert–Beer's law (Figure S6, Supporting Information). The broad absorption and relatively high ϵ value elucidated that the BAP NCs possessed the ability to serve as excellent photothermal agents. The photothermal performance of BAP NCs was studied under 1064 nm laser irradiation (1 W cm^{-2}, 10 min), and the increases in the temperature were recorded using the thermal imaging camera. As shown in Figure 2b, a remarkable increase in the temperature ($\Delta T \approx 35.6$ °C) of the BAP NCs solution (400 μg mL^{-1}) was observed within 5 min, and the corresponding infrared thermal images also reflected the consistency in the results (Figure S7, Supporting Information). Similarly, the BAP NCs showed power density-dependent photothermal efficiency (Figure S8, Supporting Information) and high photothermal stability after five cycles of laser on–off process with the maximum ΔT of BAP NCs (200 μg mL^{-1}) reached ≈26 °C within 5 min (Figure S9, Supporting Information). Additionally, the photothermal conversion efficiency (PCE) of the BAP NCs

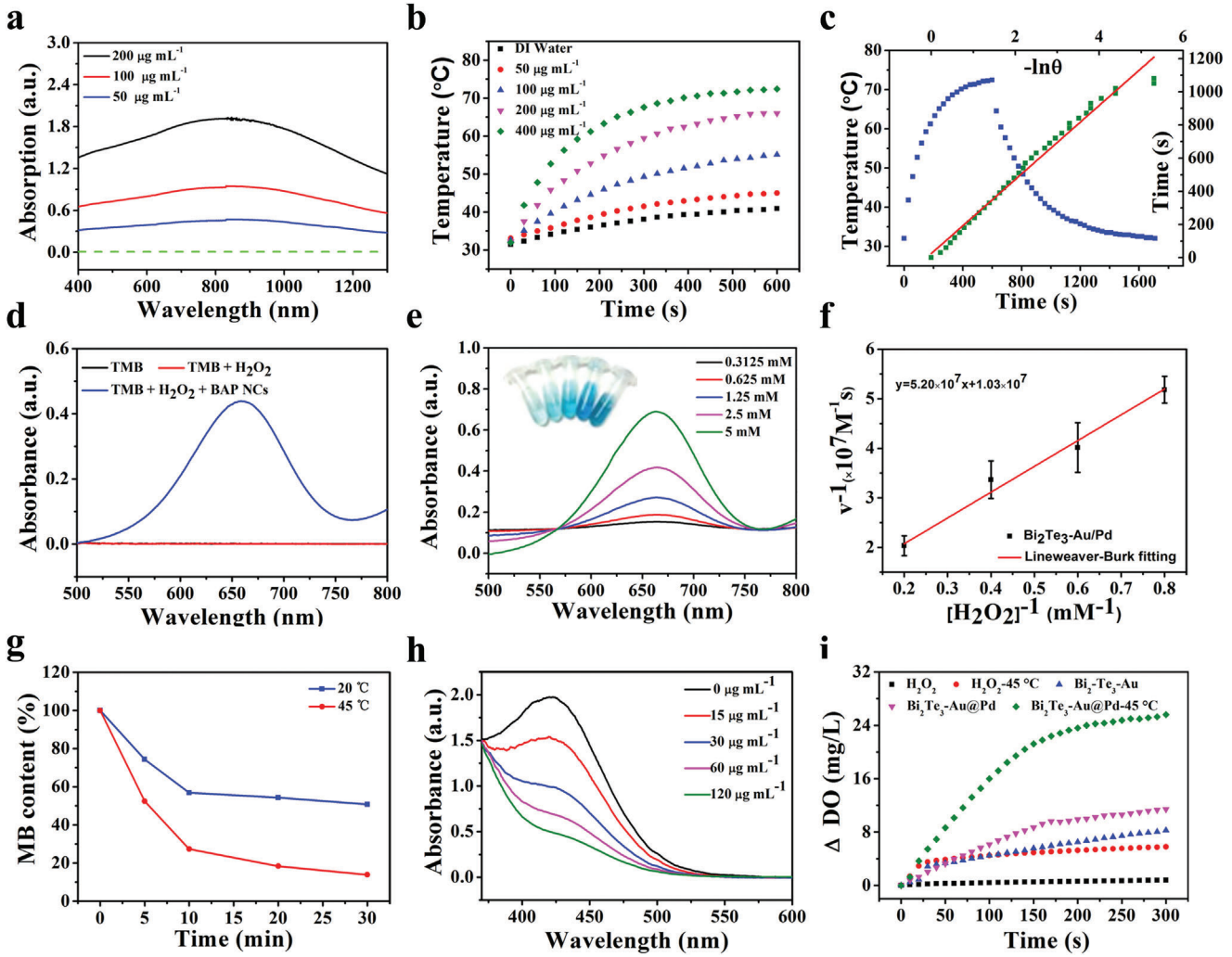

Figure 2. Photothermal and catalytic effects of the BAP NCs. a) Vis–NIR spectra of the BAP NCs dispersions at varied concentrations. b) Temperature curves of different concentrations of BAP NCs upon laser irradiation at 1064 nm (1 W cm^{-2}). c) Photothermal conversion effect of BAP NCs under 1064 nm laser irradiation (1 W cm^{-2}). d) The absorption spectra of TMB solution (black line), TMB solution in the presence of H_2O_2 (red line), and the solution after the reaction of TMB in the presence of H_2O_2 and BAP NCs incubated for 10 min (blue line). e) The absorbance spectra of TMB solution in the presence of H_2O_2 at different concentrations after incubation with the BAP NCs at room temperature. f) Lineweaver–Burk plots with H_2O_2 as the substrate. g) MB degradation due to ·OH production at different temperatures (20 and 45 °C). h) GSH consumption after being treated with different concentrations of the BAP NCs. i) The oxygen generation curves of BAP NCs with different treatments.

was determined to be ≈59.0% at 1064 nm (Figure 2c), confirming their superior photothermal conversion ability for cancer PTT.

2.3. Dual Enzyme-Like Activities and GSH Depletion Capacity of the BAP NCs

Next, the POD-like activity of the BAP NCs was investigated using 3,3,5,5-tetramethyl-benzidine (TMB) as the substrate. As shown in Figure 2d, negligible characteristic absorbance was observed in the TMB and TMB + H_2O_2 system without the BAP NCs. In contrast, the TMB + H_2O_2 + BAP NCs system with a characteristic absorption peak at 652 nm and the reaction solution showed a time-dependent increase in absorbance within 10 min (Figure S10, Supporting Information), confirming that the BAP NCs possessed POD-like activity. Moreover, as shown in Figure S11, Supporting Information, oxTMB showed the highest absorbance intensity at pH 5.4 and at 45 °C, confirming that a mild acidic environment and relatively high temperature induced the POD-like activity of the BAP NCs. More importantly, the BAP NCs exhibited excellent catalytic activity, which was 5.4- and 2.6-fold that of the Bi_2Te_3-Au NCs and the Bi_2Te_3-Pd NCs, respectively, owing to the alloy structure of Au–Pd (Figure S12, Supporting Information). To further evaluate the POD-like catalytic activity of the BAP NCs, steady-state kinetics were investigated at different concentrations of H_2O_2. Figure 2e shows the H_2O_2 concentration-dependent absorption spectrum of oxTMB and then calculates the reaction rate according to the Lambert–Beer's law (Figure 2f). The Michaelis constant (K_m) and the maximum velocity (V_{max}) were determined to be 5.05 mM and 0.97×10^{-7} M s^{-1}, respectively,

based on the Michaelis–Menten equation and the Lineweaver–Burk plot.[20] Above all, the BAP NCs showed a prominent POD-like activity for efficient •OH production. Then, the BAP NCs-mediated •OH generation was evaluated by measuring the degradation of methylene blue (MB). As shown in Figure 2g, the content was reduced by 49.3% at 20 °C and 86.1% at 45 °C upon incubation with the BAP NCs and H_2O_2 for 30 min, indicating that increase in the temperature could effectively enhance the production of •OH, confirming the feasibility of PTT enhanced FT.

The GSH scavenging effect of the BAP NCs was assessed using a typical indicator-DTNB (5,5′-dithiobis (2-nitrobenzoic)), which could be reduced by the thiol group of GSH to TNB with a characteristic absorption at 412 nm. As shown in Figure 2h and Figure S13, Supporting Information, with increasing concentration of the BAP NCs (0–120 μg mL^{-1}) and increasing reaction time (0–5 min), there was a significant increase in GSH depletion, demonstrating the excellent GSH depletion-ability of the BAP NCs.

Apart from the POD-like activity and GSH depleting capabilities of the BAP NCs, they also possessed CAT-like activity, which could induce the decomposition of H_2O_2 into H_2O and O_2. As displayed in Figure 2i, compared with the control group, the photothermal effect did accelerate the decomposition of H_2O_2. For example, at 45 °C, the variation in dissolved oxygen (ΔDO) was 5.78 mg L^{-1}, which was more than that at room temperature (0.78 mg L^{-1}). Furthermore, it should be noted that in the presence of the BAP NCs, the ΔDO was 11.42 mg L^{-1} at room temperature and 25.62 mg L^{-1} at 45 °C, indicating that the BAP NCs played a major role in the generation of O_2 . Moreover, the BAP NCs showed 1.38-fold increase in its catalytic activity when compared with Bi_2Te_3-Au, indicating that the alloy structure of Au/Pd effectively enhanced the catalytic performance of the BAP NCs. Furthermore, the catalytic O_2 production capacity of the BAP NCs at 45 °C showed 2.24-fold increase as compared to that at room temperature, which was consistent with the results for POD-like activity, demonstrating that the thermal effects could accelerate the catalytic reaction. Consequently, the BAP NCs may serve as promising candidates for effective tumor inhibition by modulating the intracellular redox homeostasis and relieving the hypoxia in the TME.

2.4. In Vitro Cytotoxicity of the BAP NCs

Before carrying out the in vitro and in vivo experiments, the BAP NCs were PEGylated with SH-PEG (sulfhydryl polyethylene glycol) to improve their biocompatibility. Next, the cytotoxicity of the BAP NCs was tested by the CCK-8 assay in 4T1 cells after different treatments. As shown in **Figure 3**a, the Bi_2Te_3 nanosheets displayed negligible cytotoxic effects on 4T1 cells even at a concentration of 200 μg mL^{-1}, demonstrating its excellent biocompatibility in vitro. Interestingly, the viability of 4T1 cells was slightly reduced upon incubation with the BAP NCs, and it might be that the BAP NCs disrupted the intracellular redox homeostasis. Comparatively, a significant decrease in cell viability (80%) was observed after treating the cells with the BAP NCs (100 μg mL^{-1}) combined with 1064 nm laser irradiation. To investigate the inhibitory effect of GSH on the BAP NCs-mediated cell death pathway, 4T1 cells were treated with the BAP NCs with or without GSH (1 mM). Then, CCK-8 assay was performed after co-culturing for 24 h. As shown in Figure S14, Supporting Information, the BAP NCs showed dose-dependent cytotoxicity. As expected, the addition of GSH significantly inhibited the cytotoxicity of the BAP NCs, suggesting that GSH played an essential role in the BAP NCs-mediated cell death. To further evaluate the antitumor effects of the combination of BAP NCs and laser-mediated PTT, the morphological changes of 4T1 cells after the different treatments were analyzed. As displayed in Figure 3b (Brightfield), the cells treated with PBS or laser irradiation remained alive, and there was no obvious change in the cell morphology, demonstrating that the dose of laser was safe, and laser alone did not affect the growth of the cells. Remarkably, the BAP NCs were efficiently internalized into the cells, and some cells were shriveled in the BAP NCs group, which could be due to the BAP NCs-mediated ferroptosis. As expected, the BAP NCs + L group exhibited severe cellular damage, which was consistent with the results from the cytotoxicity assays, indicating the potent antitumor efficacy of the combination of the BAP NCs with laser irradiation. The above results were further confirmed by calcein-AM/PI staining, indicating that the combination of the BAP NCs and 1064 nm-mediated PTT had a synergistic effect with enhanced antitumor efficacy as compared to the single treatments (Figure 3b, AM/PI).

Next, we investigated the therapeutic mechanic of the BAP NCs. We first evaluated the intracellular ROS levels in 4T1 cells using the fluorescence probe 2′,7′-dichlorofluorescein diacetate (DCFH-DA). As shown in Figure S15, Supporting Information, the control groups (PBS or laser-only) showed negligible green fluorescence, the BAP NCs group showed weak green fluorescence owing to the generation of ·OH induced by the BAP NCs, and the cells in the BAP NCs + L group showed the highest green fluorescence intensity, verifying the PTT-mediated enhancement in ROS generation.

It has been recognized that the relatively high level of GSH in the tumor cells limits ROS generation, and the efficient consumption of GSH disrupts the intracellular redox equilibrium of the tumor cells to restore the low efficiency associated with ROS-dependent therapeutics.[21] Moreover, GSH depletion induces the accumulation of LPOs by inactivating GPX4, which suppresses the transformation of highly toxic LOOH to less toxic hydroxyl fatty acids (LOH) and further facilitates ferroptosis.[22] As expected, the relative intracellular GSH level was significantly reduced (60%) after incubation with the BAP NCs, and the lowest GSH level (25.6%) was observed in the BAP NCs + L group, confirming the excellent intracellular GSH depletion capacity of the BAP NCs (Figure 3c). Furthermore, the GPX4 expression was slightly down-regulated (25.6%) and significantly inhibited (61.6%) in 4T1 cells after being treated with the BAP NCs and BAP NCs + L, respectively, which was consistent with the consumption of GSH (Figure 3d).

Encouraged by the above results, the intracellular accumulation of LPO was further evaluated. We measured the LPO levels using the Liperfluo-probe in the 4T1 cells after the different treatments. As displayed in Figure 3e, the confocal laser scanning microscopy (CLSM) images showed noticeable green fluorescence in the BAP NCs + L group and was about 2.0-fold that of the BAP NCs group (Figure 3f), which might be caused by the thermal effect. Interestingly, the ferroptosis inhibitor, ferrostation-1 (Fer-1) alleviated the accumulation of LPO, demonstrating the

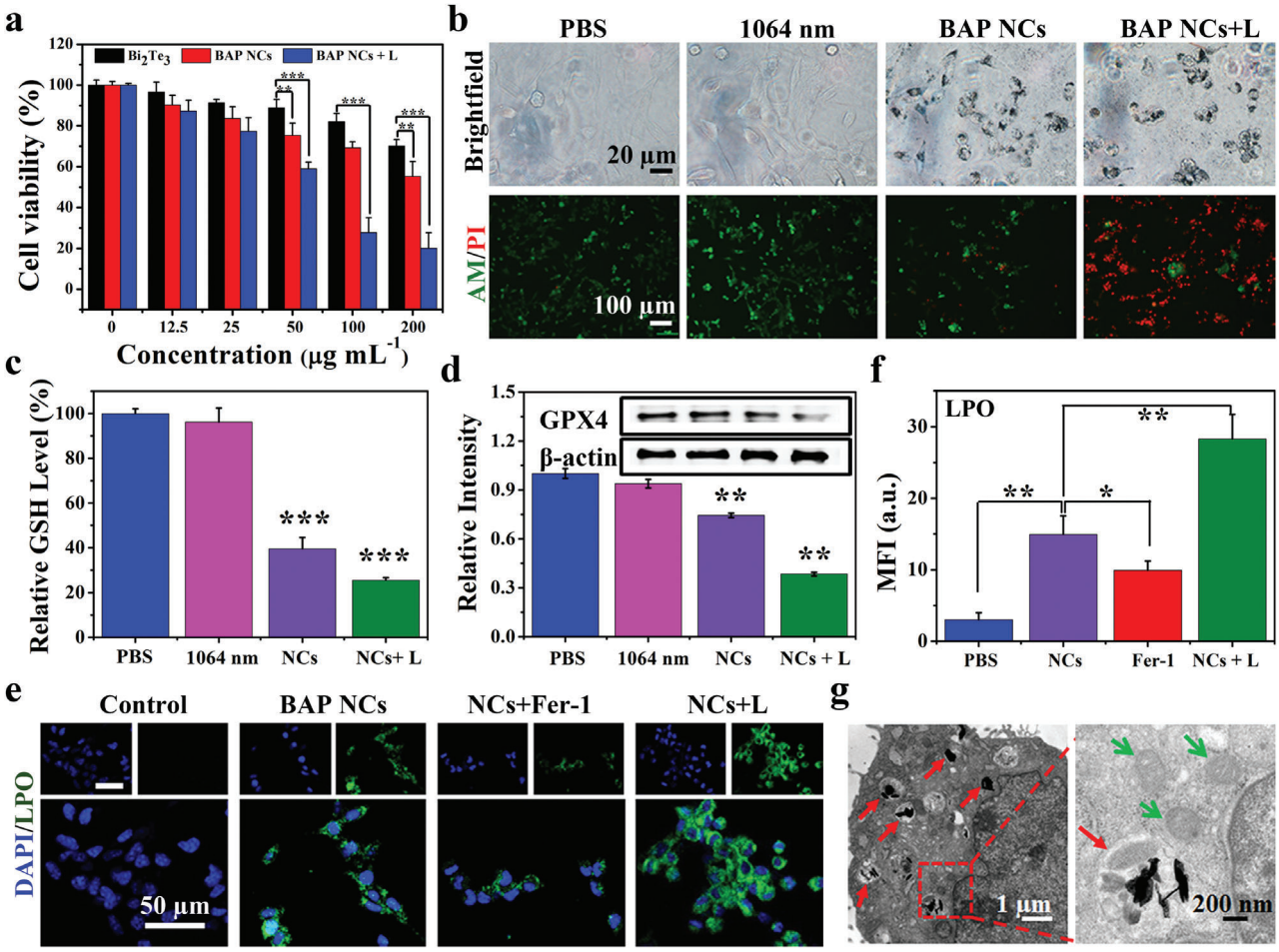

Figure 3. In vitro antitumor efficiency. a) Viability of 4T1 cells after incubation with Bi_2Te_3, BAP NCs, and BAP NCs + L (L means 1064 nm laser irradiation). b) Bright-field microscopic images of 4T1 cells and live/dead cell staining assay of 4T1 cells after various treatments. c) Intracellular GSH content after different treatments. d) GPX4 expression (inset) and relative intensity of expression in 4T1 cells after different treatments. Detection of the intracellular LPO level (e) and quantitative analysis (f) of 4T1 cells after different treatments. Scale bar: 50 μm. g) Bio-TEM images of 4T1 cells treated with the BAP NCs (red arrows refer to BAP NCs internalized by 4T1 cells, green arrows refer to the mitochondria). The data are shown as the mean ± standard deviation (s.d.) ($n = 3$), ***$p < 0.001$, **$p < 0.01$, and *$p < 0.05$.

desired accumulation of LPO mediated by the BAP NCs. Furthermore, as shown in the bio-TEM image of 4T1 cells (Figure 3g), some BAP NCs (red arrows) could be observed in the lysosomes, which indicated that the BAP NCs were internalized by the 4T1 cells through endocytosis. More importantly, the mitochondria appeared to undergo vacuolization, and the mitochondrial cristae had disappeared. Taken together, the above results demonstrated the potential of BAP NCs for promoting synergistic effects through PTT-FT.

Finally, the intracellular O_2 generation was detected by $[Ru(dpp)_3]Cl_2$ (RDPP), whose fluorescence is quenched by O_2. As shown in Figure S16, Supporting Information, compared with the control group (PBS), the fluorescence of RDPP in the BAP NCs-treated cells was lower, owing to the O_2 generation mediated by the BAP NCs through the decomposition of H_2O_2, which is overexpressed in cancer cells. Furthermore, the cells treated with the BAP NCs combined with laser showed weaker fluorescence intensity than those incubated with the BAP NCs alone, indicating that the thermal effect enhanced the generation of O_2. These results indicated that the BAP NCs possessed CAT-like activity and could alleviate hypoxia in the TME.

2.5. Evaluation of ICD In Vitro

To explore the potential of BAP NCs to activate immune responses, we first evaluated the release of damage-associated molecular patterns (DAMPs) associated with ICD, including calreticulin (CRT), adenosine triphosphate (ATP) and high mobility group protein B1 (HMGB1).[12a,23] The exposure of CRT is a potent "eat-me" signal that stimulates phagocytosis by the DCs and the release of HMGB1 promotes the maturation of DCs, which effectively activates the initial T cells and activates further adaptive immune responses. As shown in **Figure 4**a, a significant CRT exposure could be observed in the NCs and NCs + L group. Additionally, there was more green fluorescence observed in the cytoplasm of 4T1 tumor cells in the BAP NCs + L group (Figure 4b), indicating that the BAP NCs could effectively

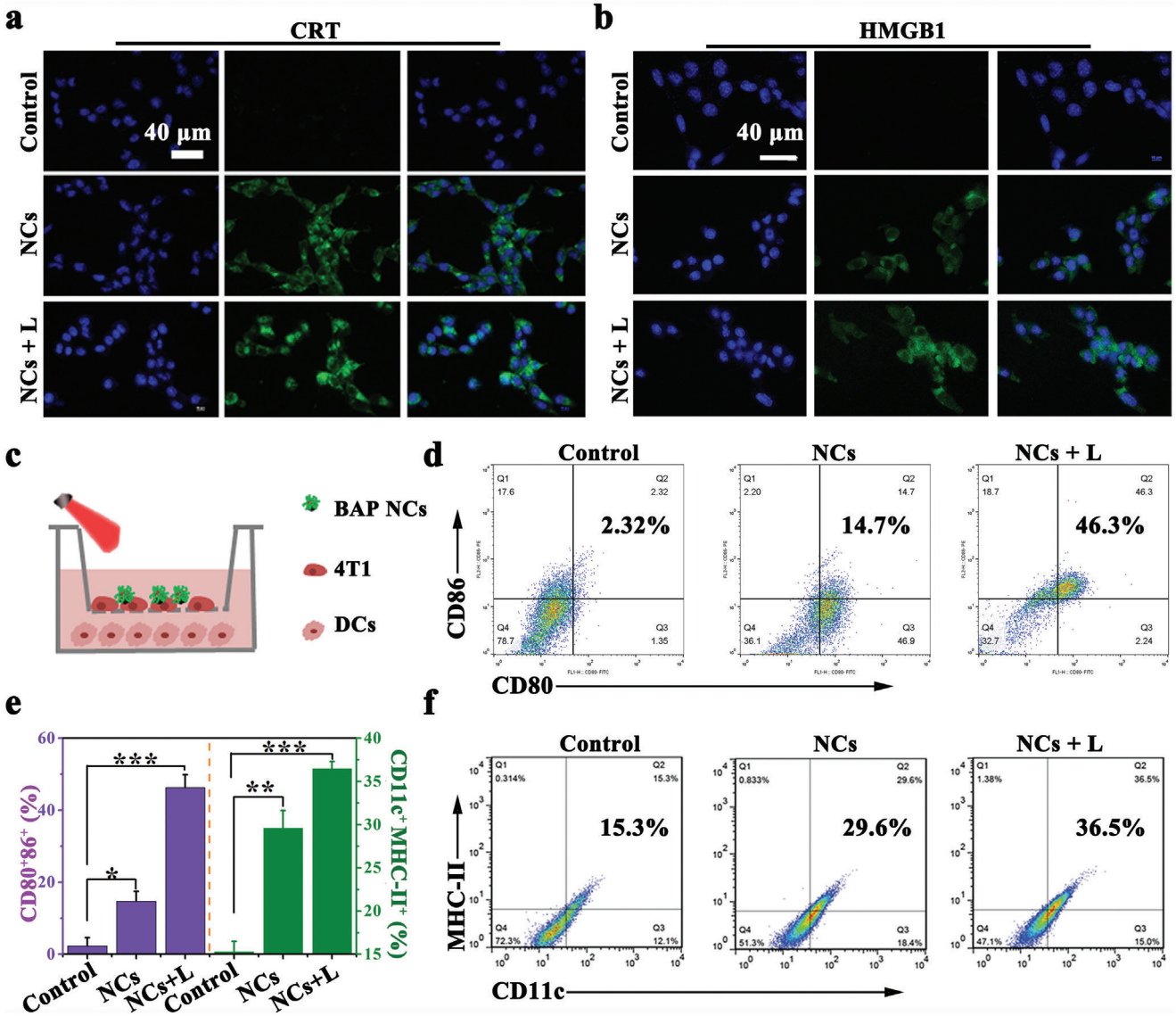

Figure 4. Evaluation of ICD in vitro. a) CRT exposure and b) HMGB1 release after different treatments. c) Schematic diagram showing the maturation of DCs stimulated through the transwell co-culture system. Representative flow cytometry plots of d) $CD80^+$ $CD86^+$ (gated on $CD11c^+$ cells), f) $CD11c^+$ $MHC\text{-}II^+$ (gated on $CD11c^+$ cells), and e) statistical analysis for the different treatment groups. The data are shown as the mean ± standard deviation (s.d.) ($n = 3$), $^{***}p < 0.001$, $^{**}p < 0.01$, and $^{*}p < 0.05$.

induce ICD under the NIR-II light irradiation. Then, the level of DCs maturation was estimated by measuring the expression of the co-stimulatory molecules CD11c, CD80, CD86 and MHC-II, through the transwell co-culture assay. As shown in Figure 4c, the DCs were seeded in the lower chamber, and 4T1 cells were seeded in the upper chamber. 4T1 cells in the treatment group were incubated with the BAP NCs for 6 h, irradiated by a 1064 nm laser, and then co-cultured with the DCs for 12 h. Afterward, the DCs were collected and stained using the APC anti-CD11c, PE anti-mouse CD86, and FITC anti-mouse CD80 antibodies (Biolegend) and analyzed by flow cytometry. The expression of CD80/86 was significantly higher in the BAP NCs-treated group (14.7%) and the BAP NCs + L group (46.3%) (Figure 4d). Moreover, an enhanced expression of CD11c/MHC-II could be observed in the BAP NCs group (29.6%) and the highest ratio of $CD11c^+$ $MHC\text{-}II^+$ was observed in the BAP NCs + L group (36.5%) (Figure 4f). Taken together, the above results confirmed the potential of BAP NCs-mediated synergistic therapy for inducing DC-related immune responses to reverse the immunosuppressive TME (Figure 4e).[24]

2.6. Photoacoustic/Thermal Imaging and Biodistribution of the BAP NCs In Vivo

Encouraged by the superior NIR absorption and PCE of the BAP NCs, we evaluated its thermal imaging and photoacoustic (PA) imaging potential. As we expected, upon the 1064 nm light

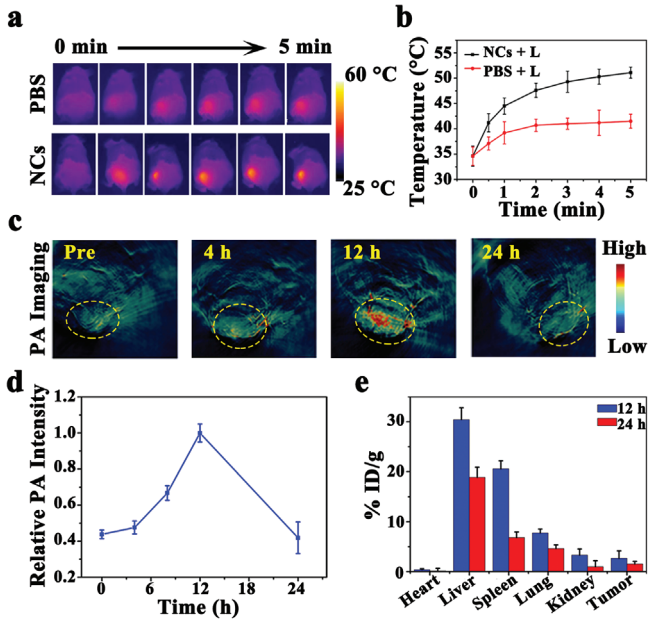

Figure 5. In vivo IR thermal/PA imaging performance and biodistribution of the BAP NCs. a) IR thermal images and b) the corresponding temperature changes in the tumor sites of tumor-bearing mice upon exposure to 1064 nm laser irradiation (1 W cm^{-2}). c) PA images and d) the corresponding quantitative analysis of the PA signal intensity of the tumor sites at different time points. e) The biological distribution of Bi in the major organs and tumors at 12 and 24 h after the intravenous injection of BAP NCs. The data are shown as the mean ± standard deviation (s.d.) ($n = 3$).

irradiation, the tumor site temperatures in the BAP NCs treated group increased rapidly to 51 °C within 5 min, suggesting the effective intratumoral enrichment of BAP NCs and their outstanding photothermal effects in the tumor. In contrast, the temperature increased negligibly in the control group (**Figure 5**a,b). As shown in Figure 5c,d, the intensity of the PA signal in the tumor site enhanced gradually after systemic administration of the BAP NCs in mice (i.v.) and reached a peak at 12 h owing to the effective accumulation of the BAP NCs due to the enhanced permeability and retention (EPR) effect. 12 h after the injection, the signals decreased gradually owing to the in vivo metabolism. The biodistribution analysis was performed to evaluate the pharmacokinetics of the BAP NCs. After systemic intravenous injection (i.v.) of the BAP NCs, the time-dependent Bi content in all the major organs and tumors was analyzed by ICP-MS. As illustrated in Figure 5e, the BAP NCs were mainly accumulated in the mononuclear phagocyte system, such as the liver and the spleen. Moreover, 2.65% ID g^{-1} at 12 h and 1.51% ID g^{-1} at 24 h of BAP NCs were accumulated in the tumor tissue, attributed to the typical EPR effect.

2.7. In Vivo Efficacy of the Combination Therapy and Antitumor Immune Response

Inspired by the excellent in vitro antitumor efficiency and effective accumulation of the BAP NCs in the tumor tissues, its therapeutic performance and immunomodulating ability in vivo were further investigated in 4T1 tumor-bearing mice. The detailed treatment schedule is shown in **Figure 6**a. 4T1 tumor-bearing mice were randomly divided into four groups ($n = 3$), including PBS, 1064 nm laser, BAP NCs and BAP NCs + 1064 nm laser. After the treatments, the in vivo therapeutic efficiency of the BAP NCs was assessed by measuring the tumor volumes every two days. It was found that a certain extent of tumor inhibition was observed after the intravenous injection of the BAP NCs, which could be attributed to the BAP NCs-mediated ferroptosis through •OH generation and GSH depletion. Of note, the tumor growth was almost suppressed in the BAP NCs + 1064 nm laser group, owing to the synergetic antitumor effects of NIR-II PTT enhanced ferroptosis (Figure 6b). Additionally, the corresponding images of the tumors also reflected the consistent therapeutic effect (Figure 6c). Moreover, the LPO level in the tumor tissues was evaluated to further demonstrate the induction of ferroptosis. As expected, green fluorescence intensity showed remarkable enhancement in the BAP NCs and BAP NCs + 1064 nm laser group compared to that of the control group, confirming the induction of ferroptosis. To further assess the therapeutic efficacy, tumor tissues were harvested from the mice after various treatments for histopathological analysis. Significant nuclear dissociation and elevated levels of cellular markers of apoptosis could be seen through the hematoxylin and eosin (H&E) and terminal deoxynucleotidyl transferase dUTP nick-end labeling (TUNEL) assay, demonstrating greater extent of necrosis in the BAP NCs + 1064 nm laser group. In contrast, negligible damage could be observed in the control group (Figure 6d), which was consistent with the above results. Taken together, effective antitumor efficiency could be achieved through the synergistic effect of NIR-II PTT/FT.

Afterward, the lung metastasis experiment was conducted to evaluate the long-term in vivo immune memory effect of the BAP NCs by rechallenging with 4T1 cells (i.v.). After the treatment, fewer pulmonary metastatic lesions were detected in the BAP NCs + 1064 nm laser group, while remarkable lung metastases (red arrows) were observed in the control group (PBS), which was further confirmed by H&E staining (Figure 6e). In more detail, the mean number of pulmonary metastatic nodules in the treatment group was 13.3-fold lower than that in the control group (Figure S17, Supporting Information). These results confirmed that the BAP NCs successfully mediated synergistic therapy and induced an immunological memory effect to suppress tumor metastasis. In addition, the body weight of the mice did not fluctuate during the treatment period (Figure S18, Supporting Information), and the H&E staining images of all the major organs (heart, liver, spleen, lung, and kidney) showed no significant histological damage after the different treatments (Figure S19, Supporting Information). To further demonstrate the biocompatibility of the BAP NCs, the hemolysis assay, biochemical indicators such as alanine aminotransferase (ALT), aspartate aminotransferase (AST) and alkaline phosphatase (ALP), and the blood routine were evaluated. As shown in Figure S20, Supporting Information, the hemolysis ratio was less than 5% at the maximum concentration (200 μg mL^{-1}) of the BAP NCs. Moreover, there was no significant difference in the measured parameters (including the blood routine and biochemical indicators) between the control and the different treatment groups (Figure S21, Supporting Information), revealing the excellent in vivo biosafety of the BAP NCs.

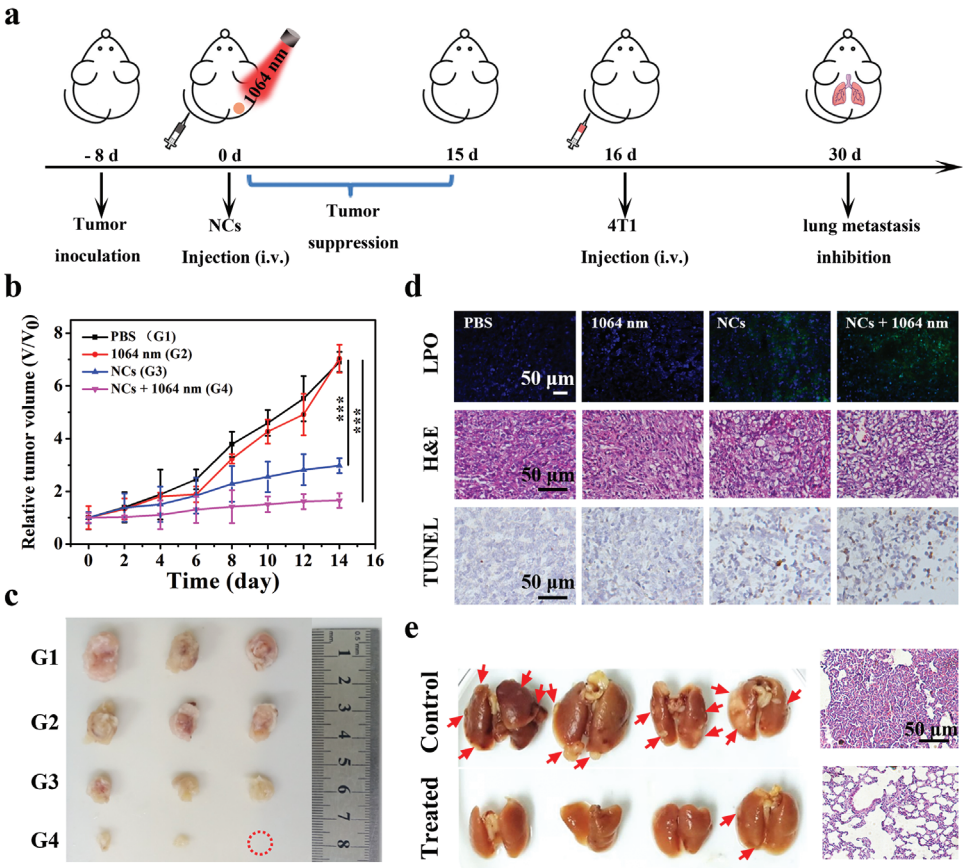

Figure 6. In vivo antitumor effects of the BAP NCs. a) Schematic illustration of the in vivo therapeutic and anti-metastasis experimental protocol. The 1064 nm laser irradiation (1 W cm^{-2}, 5 min) was performed at 4, 12, and 24 h post-injection of the BAP NCs on 0 days; the mice were rechallenged by injection (i.v.) of 4T1 cells on day 16 to assess lung metastasis. b) Tumor growth curves of mice after various treatments. c) Representative digital photos of tumor tissues from the different groups (G1: PBS, G2: 1064 nm laser, G3: BAP NCs, and G4: BAP NCs + 1064 nm laser). d) LPO, H&E, and TUNEL staining images of tumor tissues from the different groups on the 14th day. e) Photographs and H&E staining images of the lungs from mice in the different groups. Scale bar: 50 μm. The data are shown as the mean ± standard deviation (s.d.) ($n = 3$), ***$p < 0.001$, **$p < 0.01$, and *$p < 0.05$.

3. Conclusion

In summary, we developed multifunctional nanocatalyst-BAP NCs for synergistic antitumor therapy with imaging guidance. Specifically, the BAP NCs possessed NIR-II PTT and PA imaging capabilities owing to the excellent photothermal effect of the Bi_2Te_3 nanosheets. Moreover, the Au/Pd NPs were ornamented on the Bi_2Te_3 nanosheets to have POD-like, GSH depletion, and CAT-like activities to modulate the TME. We successfully demonstrated that the BAP NCs could achieve efficient synergistic anticancer NIR-II PTT and FT in vitro and in vivo, and induce a robust immune response, effectively inhibiting lung metastasis of 4T1 cells. Moreover, the BAP NCs showed excellent biosafety, making them suitable for various biomedical applications. Taken together, we believe that designing intelligent nanoenzymes to reprogram the complex TME would be a promising strategy for a desirable antitumor effect.

Supporting Information

Supporting Information is available from the Wiley Online Library or from the author.

Acknowledgements

All animal experiments were performed according to the rules of the Institutional Animal Care and Use Committee of Northeastern University (210726210101494632). This study is financially supported by the National Natural Science Foundation of China (Grant No.62075217, 11874354, 11874355, 61575194), Project of Science and Technology Agency, Jilin Province (20210101148JC, 202512JC010475440), and the State Key Laboratory of Luminescence and Applications (SKLA-2019-02, SKLA-2020-09).

Conflict of Interest

The authors declare no conflict of interest.

Data Availability Statement

The data that support the findings of this study are available in the supplementary material of this article.

Keywords

immune response, nanozymes, NIR-II photothermal therapy, oxidative stress, reactive oxygen species

Received: April 16, 2022
Revised: July 12, 2022
Published online: July 27, 2022

[1] a) H. Xiang, H. Lin, L. Yu, Y. Chen, *ACS Nano* **2019**, *13*, 2223. b) D. G. Roy, I. Kaymak, K. S. Williams, E. H. Ma, R. G. Jones, *Annu. Rev. Cancer Biol.* **2021**, *5*, 137. c) H. Phuengkham, L. Ren, I. W. Shin, Y. T. Lim, *Adv. Mater.* **2019**, *31*, 1803322.

[2] a) P. Yang, J. Tao, F. Chen, Y. Chen, J. He, K. Shen, P. Zhao, Y. Li, *Small* **2021**, *17*, 2005865. b) Y. Wei, S. Wu, Z. Liu, J. Niu, Y. Zhou, J. Ren, X. Qu, *Mater. Today* **2022**, *56*, 16. c) B. Xu, Y. Cui, W. Wang, S. Li, C. Lyu, S. Wang, W. Bao, H. Wang, M. Qin, Z. Liu, W. Wei, H. Liu, *Adv. Mater.* **2020**, *32*, 2003563.

[3] a) C. Liu, L. Luo, L. Zeng, J. Xing, Y. Xia, S. Sun, L. Zhang, Z. Yu, J. Yao, Z. Yu, O. U. Akakuru, M. Saeed, A. Wu, *Small* **2018**, *14*, 1801851. b) C. Liu, J. Xing, O. U. Akakuru, L. Luo, S. Sun, R. Zou, Z. Yu, Q. Fang, A. Wu, *Nano Lett.* **2019**, *19*, 5674. c) Y. Tao, E. Ju, J. Ren, X. Qu, *Adv. Mater.* **2015**, *27*, 1097.

[4] a) T. Chang, C. Wang, C. Chen, Y. Li, C. Hsu, H. Chang, Z. Lin, *Nano Energy* **2016**, *22*, 564. b) M. Chen, D. Kumar, C.-W. Yi, D. W. Goodman, *Science* **2005**, *310*, 291. c) O. Adeniyi, S. Sicwetsha, P. Mashazi, *ACS Appl. Mater. Interfaces* **2020**, *12*, 1973.

[5] a) Y. Huang, J. Ren, X. Qu, *Chem. Rev.* **2019**, *119*, 4357. b) C. Cao, H. Zou, N. Yang, H. Li, Y. Cai, X. Song, J. Shao, P. Chen, X. Mou, W. Wang, X. Dong, *Adv. Mater.* **2021**, *33*, 2106996.

[6] W. Zhen, Y. Liu, W. Wang, M. Zhang, W. Hu, X. Jia, C. Wang, X. Jiang, *Angew. Chem., Int. Ed.* **2020**, *59*, 9491.

[7] C. Mao, X. Liu, Y. Zhang, G. Lei, Y. Yan, H. Lee, P. Koppula, S. Wu, L. Zhuang, B. Fang, M. V. Poyurovsky, K. Olszewski, B. Gan, *Nature* **2021**, *593*, 586.

[8] a) F. Zhang, F. Li, G. H. Lu, W. Nie, L. Zhang, Y. Lv, W. Bao, X. Gao, W. Wei, K. Pu, H. Y. Xie, *ACS Nano* **2019**, *13*, 5662. b) T. Xu, Y. Ma, Q. Yuan, H. Hu, X. Hu, Z. Qian, J. K. Rolle, Y. Gu, S. Li, *ACS Nano* **2020**, *14*, 3414. c) B. Ding, P. Zheng, F. Jiang, Y. Zhao, M. Wang, M. Chang, P. Ma, J. Lin, *Angew. Chem., Int. Ed.* **2020**, *59*, 16381.

[9] W. Wang, Y. Ling, Y. Zhong, Z. Li, C. Tan, Z. Mao, *Angew. Chem., Int. Ed.* **2022**, *61*, 202115247.

[10] M. Wen, J. Ouyang, C. Wei, H. Li, W. Chen, Y. N. Liu, *Angew. Chem., Int. Ed.* **2019**, *58*, 17425.

[11] a) Z. T. Deng, C. Jiang, M. R. Younis, S. Lei, Y. L. He, H. X. Zheng, P. Huang, J. Lin, *Chin. Chem. Lett.* **2021**, *32*, 2411. b) K. Li, M. Lu, X. H. Xia, Y. Y. Huang, *Chin. Chem. Lett.* **2021**, *32*, 1010.

[12] a) Y. Ma, Y. Zhang, X. Li, Y. Zhao, M. Li, W. Jiang, X. Tang, J. Dou, L. Lu, F. Wang, Y. Wang, *ACS Nano* **2019**, *13*, 11967. b) C. Chen, Z. Wang, S. Jia, Y. Zhang, S. Ji, Z. Zhao, R. T. K. Kwok, J. W. Y. Lam, D. Ding, Y. Shi, B. Z. Tang, *Adv. Sci.* **2022**, *9*, 2104885.

[13] D. Chung, J. Yoo, Y. Sung, *Adv. Mater.* **2018**, *30*, 1704123.

[14] a) M. Chang, Z. Hou, M. Wang, M. Wang, P. Dang, J. Liu, M. Shu, B. Ding, A. A. Al Kheraif, C. Li, J. Lin, *Small* **2020**, *16*, 1907146. b) D. V. Krysko, A. D. Garg, A. Kaczmarek, O. Krysko, P. Agostinis, P. Vandenabeele, *Nat. Rev. Cancer* **2012**, *12*, 860.

[15] G. Zhang, W. Wang, X. L. Lu, X. G. Li, *Cryst. Growth Des.* **2009**, *9*, 145.

[16] M. Zhao, M. Bosman, M. Danesh, M. Zeng, P. Song, Y. Darma, A. Rusydi, H. Lin, C. W. Qiu, K. P. Loh, *Nano Lett.* **2015**, *15*, 8331.

[17] X. Li, C. Li, D. Xiang, C. Zhang, L. Xia, X. Liu, F. Zheng, X. Xie, Y. Zhang, W. Chen, *Appl. Catal. B* **2019**, *253*, 263.

[18] X. Chen, Y. Shen, P. Zhou, X. Zhong, G. Li, C. Han, D. Wei, S. Li, *Sens. Actuators, B* **2019**, *289*, 160.

[19] a) B. Liu, K. Li, Y. Luo, L. Gao, G. Duan, *Chem. Eng. J.* **2021**, *420*, 129881. b) Y. Xu, D. Wu, P. Deng, J. Li, J. Luo, Q. Chen, W. Huang, C. M. Shim, C. Jia, Z. Liu, Y. Shen, X. Tian, *Appl. Catal. B Environ.* **2022**, *308*, 121223.

[20] a) H. Lineweaver, D. Burk, *J. Am. Chem. Soc.* **1934**, *56*, 658. b) X. Sun, S. Guo, C. S. Chung, W. Zhu, S. Sun, *Adv. Mater.* **2013**, *25*, 132.

[21] a) Y. Sang, F. Cao, W. Li, L. Zhang, Y. You, Q. Deng, K. Dong, J. Ren, X. Qu, *J. Am. Chem. Soc.* **2020**, *142*, 5177. b) Z. Zhao, W. Wang, C. Li, Y. Zhang, T. Yu, R. Wu, J. Zhao, Z. Liu, J. Liu, H. Yu, *Adv. Funct. Mater.* **2019**, *29*, 1905013. c) L. Chaiswing, W. Zhong, J. J. Cullen, L. W. Oberley, T. D. Oberley, *Cancer Res.* **2008**, *68*, 5820.

[22] a) W. S. Yang, R. SriRamaratnam, M. E. Welsch, K. Shimada, R. Skouta, V. S. Viswanathan, J. H. Cheah, P. A. Clemons, A. F. Shamji, C. B. Clish, L. M. Brown, A. W. Girotti, V. W. Cornish, S. L. Schreiber, B. R. Stockwell, *Cell* **2014**, *156*, 317. b) B. Hassannia, P. Vandenabeele, T. V. Berghe, *Cancer Cell* **2019**, *35*, 830.

[23] Q. Chen, M. Chen, Z. Liu, *Chem. Soc. Rev.* **2019**, *48*, 5506.

[24] X. Fang, X. Wu, Z. Li, L. Jiang, W. S. Lo, G. Chen, Y. Gu, W. T. Wong, *Adv. Sci.* **2021**, *8*, 2003041.